Acta Biomaterialia 120 (2021) 167–180

Contents lists available at ScienceDirect

Acta Biomaterialia

journal homepage: www.elsevier.com/locate/actbio

Full length article

On the amorphous layer in bone mineral and biomimetic apatite: A combined small- and wide-angle X-ray scattering analysis☆

Federica Bertolotti[a], Francisco J. Carmona[a], Gregorio Dal Sasso[b], Gloria B. Ramírez-Rodríguez[a,c], José Manuel Delgado-López[c], Jan Skov Pedersen[d], Fabio Ferri[a], Norberto Masciocchi[a,*], Antonietta Guagliardi[b,*]

[a] Department of Science and High Technology and To.Sca.Lab, University of Insubria, Via Valleggio 11, I-22100 Como, Italy
[b] Institute of Crystallography and To.Sca.Lab, Consiglio Nazionale delle Ricerche, Via Valleggio 11, I-22100 Como, Italy
[c] Department of Inorganic Chemistry, University of Granada, Av. Fuentenueva S/N, E-18071 Granada, Spain
[d] Department of Chemistry and Interdisciplinary Nanoscience Center (iNANO), Aarhus University, Gustav Wieds Vej 14, 8000 Aarhus, Denmark

ARTICLE INFO

Article history:
Received 28 January 2020
Revised 4 April 2020
Accepted 13 April 2020
Available online 11 May 2020

Keywords:
Bone minerals
Biomimetic apatite
Amorphous surface layer
SAXS
WAXTS
Debye scattering equation

ABSTRACT

The occurrence of an amorphous calcium phosphate layer covering the crystalline apatite core has been suggested to be an intrinsic feature of both bone mineral and synthetic biomimetic analogs. However, an exhaustive quantitative picture of the amorphous-crystalline relationship in these materials is still missing. Here, we present a multiple scale modelling that combines small-angle X-ray scattering (SAXS) and synchrotron wide-angle X-ray total scattering (WAXTS) analyses to investigate the amorphous-crystalline spatial interplay in bone sample and biomimetic carbonated nano-apatites. SAXS analysis indicates the presence of a single morphology consisting of tiny nanoplates (NPLs) and provides a measure of their thickness (falling in the 3–5 nm range). WAXTS analysis was performed by developing atomistic models of apatite NPLs incorporating lattice strain, mostly attributed to the carbonate content, and calculating the X-ray patterns using the Debye Scattering Equation. Upon model optimization, the size and strain parameters of the crystalline platelets were derived and the amorphous component, co-existing with the crystalline one, separated and quantified (in the 23–33 wt% range). Notably, the thickness of the apatite core was found to exhibit nearly null (bone) or minor (< 0.5 nm, biomimetic samples) deviations from that of the entire NPLs, suggesting that the amorphous material remains predominantly distributed along the lateral sides of the NPLs, in a core-crown-like arrangement. The lattice strain analysis indicates a significant stiffness along the *c* axis, which is comparable in bone and synthetic samples, and larger deformations in the other directions.

Statement of Significance

Current models of bone mineral and biomimetic nanoapatites suggest the occurrence of an amorphous layer covering the apatitic crystalline nanoplates in a core-shell arrangement. By combining X-ray scattering techniques in the small and wide angle regions, we propose a joint atomic-to-nanometre scale modelling to investigate the amorphous-crystalline interplay within the nanoplates. Estimates are extracted for the thickness of the entire nanoplates and the crystalline core, together with the quantification of the amorphous fraction and apatite lattice strain. Based on the thickness matching, the location of the amorphous material mostly along the edges of the nanoplates is inferred, with a vanishing or very thin layer in the thickness direction, suggesting a core-crown-like arrangement, with possible implications on the mineral surface reactivity.

☆ Part of the Special Issue on Biomineralization: From Cells to Biomaterials, associated with the BIOMIN XV: 15th International Symposium on Biomineralization, held at the Ludwig Maximilian University, Sept 9-13, 2019, organized by Wolfgang Schmahl and Erika Griesshaber.

* Correspondence authors.
E-mail addresses: norberto.masciocchi@uninsubria.it (N. Masciocchi), antonella.guagliardi@ic.cnr.it (A. Guagliardi).

https://doi.org/10.1016/j.actbio.2020.04.026
1742-7061/

1. Introduction

The occurrence of a persistent amorphous layer covering the nanocrystalline apatite core as an intrinsic feature of the mineral component of bone is a long-debated subject. To date, there is a wide consensus on that the mature mineral appears in the form of thin platelets (1-5 nm) of apatite crystals [1–3], having variable width (10-40 nm) and length (20-100 nm), structurally resembling hydroxyapatite of geological origin, $Ca_{10}(PO_4)_6(OH)_2$, compared to which various compositional and structural defects occur. These defects include calcium and hydroxyl deficiencies [4] and a number of ionic substitutions (known to proceed via Ca^{2+} replacement or by anionic exchange), leading to peculiar lattice and structural distortions unmet in the reference hydroxyapatite crystal phase. Among the exogenous ions, CO_3^{2-} is by far the most abundant (from 4% up to 9% by weight), typically replacing PO_4^{3-} groups (B-type) but also OH^- ions (A-type), and likely being the most critical replacement in directing crystallization/dissolution processes [5–7].

The current and most accredited view agrees with an additional non-apatitic environment, closely related to an hydrated amorphous calcium phosphate (ACP) phase, encapsulating the apatite nanoplate in a core-shell structure [8–14]. Experimental evidence of such structurally disordered coating (or non-apatitic environments) has been provided over the years by different and complementary techniques including spectroscopy (solid-state nuclear magnetic resonance, SS-NMR, and infrared, IR, spectroscopies) [8,11,13–15], microscopy (particularly High-Resolution Transmission Electron Microscopy, HR-TEM) [9] and diffraction (the latter based on either reciprocal or direct space methods of analysis, such as the Radial Distribution Function) [11,16,17]. Aiming at clarifying the nature, origin and time evolution of this ACP-like surface layer, experiments have been carried out both on bone mineral (at the earliest stages of formation and in the mature tissue) and on synthetic biomimetic samples that mimic the crystal size, morphology and carbonation content of the biogenic phase.

Meanwhile, many parallel studies have highlighted the role of an amorphous calcium phosphate precursor phase in the formation of bone apatite and synthetic analogues [11,18–22]. Despite that the amorphous-to-apatite transformation still needs to be fully understood, a dual scenario arose on the origin of the amorphous layer, which might result from either a not-yet transformed fraction of the ACP precursor or a persistent surface coating. More precise knowledge has been raised progressively mainly by reconciling the ACP-like nature with the surface properties of biogenic and biomimetic apatite [12–14]. Such advances have great relevance to the comprehension of the biomineralization mechanisms and implications in bio-inspired materials preparation for a number of applications [23–25]. The nature of the surface is fundamental in controlling the chemical reactivity and the mineral ability to bind proteins and molecules, involving a significant amount of water molecules that are suggested to play a role in mediating the mineral-organic matrix interactions and, recently, also in orienting bone apatite platelets [11,26,27].

Nonetheless, providing a comprehensive quantitative picture of the apatite-ACP core-shell system and the mutual extent of the two components remains a difficult task, which stimulates progress in developing new experimental and computational tools. An amorphous 1-2 nm thick surface layer has been imaged in synthetic apatite nanocrystals by ultra-high resolution TEM [9]; however, investigation of the amorphous coating by HRTEM is rather uncommon because of the ACP instability under the electron beam. Moreover, the information derived therefrom is typically obtained on individual synthetic nanocrystals rather than on their ensemble. (Semi)-quantitative models have been proposed, based on NMR spectroscopies and chemical composition considerations, pointing to a disordered hydrated surface layer featuring a high concentration of hydrogen phosphate anions, both in synthetically precipitated [8] and mature bone mineral [14] samples. The thickness of such layer was estimated to be about 10% of each linear crystal dimension in the synthetic material (about 1 nm x 1 nm x 4 nm for a TEM-determined crystal size of 10 nm x 10 nm x 40 nm). A slightly smaller absolute value (0.8 nm) was determined for a 4 nm thick bone mineral particle by a combination of dedicated SS-NMR techniques [14].

With the present work, we propose a quantitative multiple scale approach combining small-angle X-ray scattering (SAXS) analysis and synchrotron wide angle X-ray total scattering (WAXTS) modelling, based on the Debye Scattering Equation (DSE) [28,29]. By this combination we provide results at an unprecedented detail level that contributes to further clarify the subject. SAXS is currently a consolidated technique for investigating bone tissue and its heterogeneous hierarchical structure at the different levels of organization, particularly when used in scanning mode [20,30–32]. SAXS analysis greatly contributed to the determination of the size and morphology of the bone mineral [30,33–41]. However, the technique is blind to the atomic scale structure and, considering also the poor density contrast, ineffective to differentiate the crystalline core from an amorphous shell of similar composition. Atomic-scale features are intrinsically accessed by wide-angle X-ray scattering methods. Indeed, X-ray and neutron powder diffraction (XRPD/NPD) and the Rietveld refinement method [42–44] are commonly applied for characterizing bone/biomimetic apatite, addressing lattice parameters (varying with carbonation) and coherent domain extension. Recently reported scanning XRPD [45–49] and simultaneous SAXS/WAXS experiments [50–53] also provided interesting advances in terms of spatial and time evolution of bone and engineered systems. In this regard, worth to mention are scanning TEM studies and 3D tomographic reconstruction of bone mineral at higher-level of organization, enabling spatial morphological variations of the mineral and its association with the organic matrix to be visualized, eventually suggesting that platelets form upon merging of acicular apatite nanocrystals [54,55].

Synchrotron data collected in WAXTS mode enable the strict control (and safe removal) of all extra-sample scattering contributions and allow the total (Bragg and diffuse) scattering from the sample to be accounted for, by either reciprocal-space pattern modelling (via the DSE method) or the (more popular) Radial or Pair Distribution Function analysis of the Fourier-transformed signal in direct space [56,57]. Using the DSE approach, the scattering from the defective apatite core and the ACP-like shell can be disentangled and quantitatively treated [21]. However, their mutual spatial relationships cannot be directly assessed. Moreover, since the DSE-based analysis relies on atomistic models of nanocrystals integrating also size and shape details (jointly to crystal structure and defects), multiple atomic-to-nanometer scale information is simultaneously provided. Despite of such great advantage, DSE-based methods have rarely been considered in the field of biomineralization [21], owing to their intrinsically high computational cost. Recent advances in this regard have opened new perspectives [29,58].

We have performed a combined SAXS/WAXTS analysis relying on forefront modelling of both types of data, here developed on a powdered rabbit bone and two biomimetic nano-apatites. The synthetic materials were selected based on their carbonate content close to the bone mineral level. The study includes the construction of atomistic models of highly defective apatite nanoplates (NPLs), calculations based on a fast implementation of the Debye scattering equation and independent in-depth analysis of SAXS (Section 3.2) and WAXTS (Section 3.3) data. Implications of the results presented in this work in bone mineralization and in the field of synthetic analogues are briefly introduced (Section 3.4). For bone, results refer to average properties of the mineral component

and disregard spatial variations (either chemical or morphological) due to the hierarchical bone organization [55,59].

2. Materials and Methods

2.1. Materials and sample preparation

Rabbit Bone sample. No animals used in this research were sacrificed for research purposes. Femur bone of a young (8 months old) rabbit was obtained from a slaughterhouse. The femur was repeatedly washed with pure ethanol and ultrapure water, then carefully milled until obtaining a fine powder. The sample was stored at -18 °C before being used for WAXTS data collection.

Synthetic samples. All materials were commercially available and used without further purification. Calcium chloride dihydrate ($CaCl_2{\cdot}2H_2O$, BioXtra, ≥99.0 % pure), anhydrous di-potassium hydrogen phosphate (K_2HPO_4, ACS reagent, ≥98.0), sodium carbonate (Na_2CO_3, BioXtra, ≥99.0 % pure) and anhydrous di-ammonium hydrogen phosphate ($(NH_4)_2HPO_4$, ACS reagent, ≥98.0) were supplied by Sigma-Aldrich. Two biomimetic samples (cAp1 and cAp2) exhibiting carbonate contents comparable to that in bone mineral were selected, the preparation of which varied in the phosphate salt and maturation time. Two aqueous solutions (1:1 v/v, 100 mL total) of (i) 0.2 M $CaCl_2{\cdot}2H_2O$ and (ii) 0.1 M $Na_2CO_3 + 0.12$ M K_2HPO_4 (sample labelled cAp1) or $(NH_4)_2HPO_4$ (sample labelled cAp2) were mixed at room temperature. The mixture was introduced in a glass bottle sealed with a screw cap (Duran) and heated at 37 °C for 24 h (cAp1) and 96 h (cAp2). Powders precipitated at 5 minutes for the synthetic condition of cAp2 were also prepared as reference for the fully amorphous material. The resulting solids were collected by centrifugation (10 min at 5000 rpm), washed with water (1 × 100 mL, 1 × 50 mL), freeze-dried (LyoQuest, Telstar, Spain) and stored at room temperature.

2.2. Materials characterization

2.2.1. Compositional, spectroscopic and microscopic characterization

The chemical composition (Ca, P, Na and K) of the synthetic samples was quantified by Inductively coupled plasma optical emission spectrometry (ICP-OES, Perkin-Elmer OPTIMA 8300, at the Centre of Scientific Instrumentation, University of Granada, CIC-UGR). 20 mg of each sample were dissolved in 2 mL of ultrapure nitric acid and then diluted up to 100 mL with Milli-Q water. The emission wavelengths were 317.93 nm (Ca), 213.62 nm (P), 589.59 nm (Na) and 766.49 nm (K). Carbon (C) content was quantified by a Thermo Scientific Flash 2000 Organic Elemental Analyzer equipped with a microbalance (XP6, Mettler Toledo, CIC-UGR).

Fourier Transform Infrared spectroscopy (FT-IR) data were collected with a Bruker Tensor 27 spectrophotometer. 2 mg of the sample were mixed with 150 mg of KBr and pressed to form a pill. The spectra were collected with a spectral resolution of 2 cm^{-1} by accumulating 32 scans in the 4000–450 cm^{-1} range.

Transmission Electron Microscopy (TEM) images were collected with a LIBRA 120 PLUS (Carl Zeiss SMT) operating at 120 kV. Synthesized nanoparticles were carefully dispersed in ethanol with ultrasound and then few drops were deposited on 200 mesh copper grids covered with thin amorphous carbon films.

2.2.2. Small-angle X-ray scattering (SAXS)

SAXS measurements were performed at the in-house instrument at Aarhus University [60], equipped with a rotating Cu anode, a side-by-side Montel multilayer mirrors (monochromatizing and focusing the beam) and a Bruker AXS Vantec 500 detector. Thin layers of the sample powders were picked up by matte acetate Scotch tape and mounted in the beam in the integrated vacuum of the SAXS instrument. A piece of the same tape was measured and subtracted as background. The data treatment was done using the in-house developed SUPERSAXS program package (C.L.P. Oliveira and J.S. Pedersen, unpublished). Conventional SAXS analysis was carried out by calculating the scattered intensity of the biomimetic and bone samples as the product of a disc form factor, $\langle P(Q)\rangle$ [33] and a structure factor $S(Q)$. A random-phase approximation (RPA) was used for accounting for concentration effects [61]. Details on SAXS data collection, reduction and modelling are provided as Supplementary Methods.

2.2.3. Synchrotron wide angle X-ray total scattering (WAXTS) characterization

WAXTS experiments were performed at the X04SA-MS beamline of the Swiss Light Source (Paul Scherrer Institut, Villigen, CH) [62], by loading powders of bone, cAp1 and cAp2 in glass capillaries (Ø = 0.5 mm, 0.01 nm thick walls). The beam energy was set at 16 keV (biomimetic samples) and 22 keV (bone). Raw data were corrected for systematic errors (zero-position and offsets) and absorption effects; scattering contributions from capillary and environment were independently collected and subtracted by taking wall capillary and sample absorption into account, as described in the Supplementary Methods. The Debye scattering equation (DSE) [28,29,57,63] was used to model WAXTS and SAXS data. Atomistic models of Ca deficient apatite nanoplates (NPLs) were generated, from which the total X-ray scattering pattern in reciprocal space (both Bragg and diffuse intensities) was computed. Details of the equation are provided as Supplementary Methods. The DSE models used for SAXS and WAXTS analysis of bone and biomimetic samples are described in the Results section, where strengths and shortcomings are also discussed. For the bone sample, Rietveld analysis was also performed using the software TOPAS Academic Program V.6 (A. Coelho, 2016, Coelho Software, Brisbane, Australia) and the phenomenological approach based on spherical harmonics to model needle shaped crystals and an anisotropic strain obeying the hexagonal crystal symmetry. Details are provided in the Supplementary Methods.

2.2.4. Statistical analysis

Standard uncertainties or estimated standard deviations (esd's) of values quoted in the Tables are obtained as follows. For the chemical compositions, Ca, P, K and Na content was measured three times in each sample. Esd's are provided in Table S1. For conventional SAXS analysis, model parameters optimization was performed using weighted least-squares methods, as detailed in the Supplementary Methods. A maximum of five parameters were refined against 520 (cAp1 and cAp2) or 260 (bone) data points [I(Q) values]. The corresponding esd's are provided in the pertinent Tables (Table 1 and Table S2). For the DSE analysis, model parameters optimization was performed using the Simplex method, as detailed in the Supplementary Methods. For SAXS-DSE analysis up to four parameters were refined against 440 (cAp1, cAp2) data points. For WAXTS-DSE analysis, up to 11 parameters were adjusted using 19430 (bone) and 30550 (cAp1, cAp2) data points. Both structural (mainly isotropic thermal vibration and site occupancy factors) and microstructural (size and shape) parameters were relaxed; two additional scale parameters were refined by least-squares. Esd's of model parameters were calculated using the curvature of the χ^2 hypersurface about the minimum and are provided in the pertinent Tables (Table 2, Table 3 and Table S2).

3. Results and discussion

3.1. Analytical characterization of biomimetic samples

Chemical analysis of the biomimetic samples (Table S1) indicates Ca deficiency and/or phosphate substitutions (Ca/P = 1.64 in

Table 1
SAXS analysis based on a finite disc-shape model: number-based average thickness (T_N), its relative dispersion (σ/T_N) and disc diameter (D_N), according to either a Schulz-Zimm or a lognormal distribution function. The ν parameter describes concentration effects; the coefficient (P) is the exponent of the power law used to describe aggregation effects at very low Q values in bone. Values in parentheses are the parameter uncertainties (esd's) as derived by the least-squares optimization. DSE-based SAXS analysis for an atomistic disc-shape model considering polydispersity of T_N jointly to either monodisperse (*mono*) or polydisperse (*poly*) D_N values. Related esd's are given in parentheses.

Conventional	T_N (*nm*)	σ/T_N	D_N (*nm*)	ν	P	χ^2
	Schulz-Zimm					
cAp1	2.29(2)	0.50(1)	43.8(1)	2.32(6)	-	3.08
cAp2	3.97(2)	0.45(6)	41.2(8)	-0.35(2)	-	3.73
Bone	2.25(1)	0.73(2)	100.0[a]	$1.3(3)\cdot10^3$	2.92(5)	6.26
	Lognormal					
cAp1	2.52(1)	0.53(1)	42.8(2)	2.35(6)	-	3.47
cAp2	4.26(1)	0.51(1)	41.2(9)	-0.31(2)	-	4.31
DSE *mono*	T_N (*nm*)	σ/T_N	D_N (*nm*)	σ/D_N	-	χ^2
cAp1	2.5(1)	0.35(1)	44.0[a]	0.01[b]		7.30
cAp2	4.4(2)	0.47 [c]	50.0[a]	0.01[b]		3.64(*)
DSE *poly*	T_N (*nm*)	σ/T_N	D_N (*nm*)	σ/D_N	-	χ^2
cAp1	2.54(4)	0.53(2)	12.0[a]	0.56 [c]		0.87(*)
cAp2	4.4(1)	0.43 [c]	50.0[a]	0.30 [c]		5.42

[a] Fixed parameter,
[b] constrained parameter,
[c] esd $< 10^{-3}$, (*) best DSE model.

cAp1, 1.58 in cAp2), in line with typically reported values, and CO_3^{2-} contents (in the 6.45 – 7.40 wt% range) comparable to bone levels [7]. FTIR spectra of cAp1 and cAp2 (Fig. S1) show the typical PO_4^{3-} vibrational modes of apatite: the triply degenerated mode (ν_3PO_4) at ~1032 cm^{-1} with shoulders at 1046 cm^{-1} and 1087 cm^{-1}, the symmetric stretching mode (ν_1PO_4) at 962 cm^{-1} and the triply degenerated bending mode (ν_4PO_4) at 561 cm^{-1}, 574 cm^{-1} (shoulder) and 602 cm^{-1} [64]. CO_3^{2-} vibrational modes are found at 1450 cm^{-1}, 1409 cm^{-1} and at 871 cm^{-1}, indicating the partial substitution of PO_4^{3-} by carbonate ions in the apatite crystal lattice (B-type), at 1472 cm^{-1} (due to CO_3^{2-} replacing PO_4^{3-} ions without an adjacent OH^-), with very minor OH^- groups (A-type) replacement (weak shoulders at 1495 cm^{-1} and 1525 cm^{-1} are found in cAp2) [3]. TEM images of cAp1 and cAp2 (Fig. S1) show the platy-like morphology of the precipitated particles in both samples. Larger aggregates are observed in cAp1. A thorough investigation of the nanoparticle morphology was carried out by SAXS analysis.

3.2. Nanoparticle size and morphology by SAXS analysis

SAXS analysis was used to access reliable information about the morphology and size of the mineral particles regardless of their amorphous or crystalline nature. In bone, information about the collagen matrix has been disregarded (the much lower electron density and the high degree of mineralization of the bone sample make it nearly negligible) and our analysis focusses only on the mineral component. For the biomimetic materials, considering that apatite typically crystallizes in gradual stages of maturation from a transient amorphous precursor (appearing as spheroidal particles), for the powders of the present study co-existence of multiple morphologies might be expected. In this regard, the presence of an amorphous fraction was certified by WAXTS analysis (as detailed in Section 3.3) either in our biomimetic cAp1 and cAp2 or in the bone samples. Therefore, SAXS analysis was also addressed to answer the question whether particles in these samples appear with single or distinct morphologies. The analysis was performed using a classical modelling originally developed for biological samples [33,37], relying on analytical form factors, by assuming a constant electron density within the geometrical envelope of each nanoparticle. An alternative modelling based on the DSE method is additionally presented for cAp1 and cAp2.

Table 3
Comparison of (mass-average) T_M values from SAXS analysis (T_{SAXS}, measuring the thickness of the entire core-shell platelets) and from WAXTS analysis (T_{Ap} measuring the thickness of core apatite only, *Ap*). T_{SAXS} refers to the disc-shape model for bone (see Table S2) and to the average of all SAXS models for cAp1 and cAp2 (see Fig. 6); T_{Ap} refers to the best model in Fig. 5; $\Delta T_1 = (T_{SAXS} - T_{Ap})$. ACP wt% is obtained by WAXTS analysis (see text for details).

	Thickness SAXS *vs* WAXTS *(Ap)*				*ACP*, wt%
	T_{SAXS}, nm	T_{Ap}, nm	$\Delta T_1/2$, nm	ΔT_1 / T_{SAXS}, %	
cAp1	3.09(1)	2.9(1)	0.09(5)	5.8	31.5
cAp2	5.11(6)	4.33(2)	0.39(3)	15.3	23.3
bone	3.71(3)	3.7(2)	0.0(1)	0.0	31.6

3.2.1. Conventional SAXS analysis with disc-shape and thickness polydispersity

Conventional SAXS analysis provided a distinctive platy morphology of bone and biomimetic samples, therefore excluding the occurrence of other morphologies. Information on the average thickness (T) was obtained through a finite disc-shape model having much larger and monodisperse diameter (D); polydispersity of T was introduced according to either a Schulz-Zimm or lognormal distribution [65] and concentration effects treated according to the RPA structure factor model [33]. For the bone sample, a power law scattering was also included to describe the scattering at the lowest angles. Model parameters adjusted by least-squares methods against experimental data are provided in Table 1, where sizes are given as number-based averages (mass-based values are available in Table S2). Fig. 1a shows the corresponding best fits from the Schulz-Zimm distribution. Notably, the average disc thickness varies in the 2.3–4.0 nm range for the three samples, with moderate to large polydispersity ($\sigma/T \geq 45\%$). The thickness in bone is in line with the values reported for different animals using a similar model [37]. The disc diameter in bone ($D \sim 100.0$ nm) is larger than in synthetic apatite ($D \sim 41.0$ nm). The bone model using the lognormal distribution lead to extremely large, unrealistic, thickness dispersion ($\sigma/T \geq 100\%$) and was discarded from subsequent discussion. The analysis also shows a striking difference between biomimetic and biological samples in terms of concentration effects (measured by the ν parameter in Table 1), which is quite low

Table 2
Size and strain results from the best selected WAXTS-DSE NPL model of apatite, corresponding to the $b/a = 9$ (bone), $b/a = 5$ (cAp1) and $b/a = 7$ (cAp2). Mass-based average thickness (T_{Ap}), width (W_{Ap}) and length (L_{Ap}), relative dispersions ($\sigma/W = \sigma/T$ and σ/L) and *GoF* values. Esd's are in parentheses. Anisotropic strain parameters (ε_a, ε_b, ε_c) result from the analysis shown in Fig. 4.

	T_{Ap} (*nm*)	W_{Ap} (*nm*)	$\sigma/T_{Ap}=\sigma/W_{Ap}$	L_{Ap} (*nm*)	σ_L/L_{Ap}	ε_a (%)	ε_b (%)	ε_c (%)	*GoF*
bone	3.7(2)	38.6(1)	0.43(5)	24.6(3)	0.6(2)	0.9	0.5	0.4	3.37
cAp1	2.87(1)	16.60(9)	0.33[a]	17.8(3)	0.74(4)	2.2	1.0	0.4	5.22
cAp2	4.33(1)	34.97(1)	0.46[a]	18.00(5)	0.55[a]	1.5	1.0	0.3	6.96

[a] Esd $< 10^{-3}$.

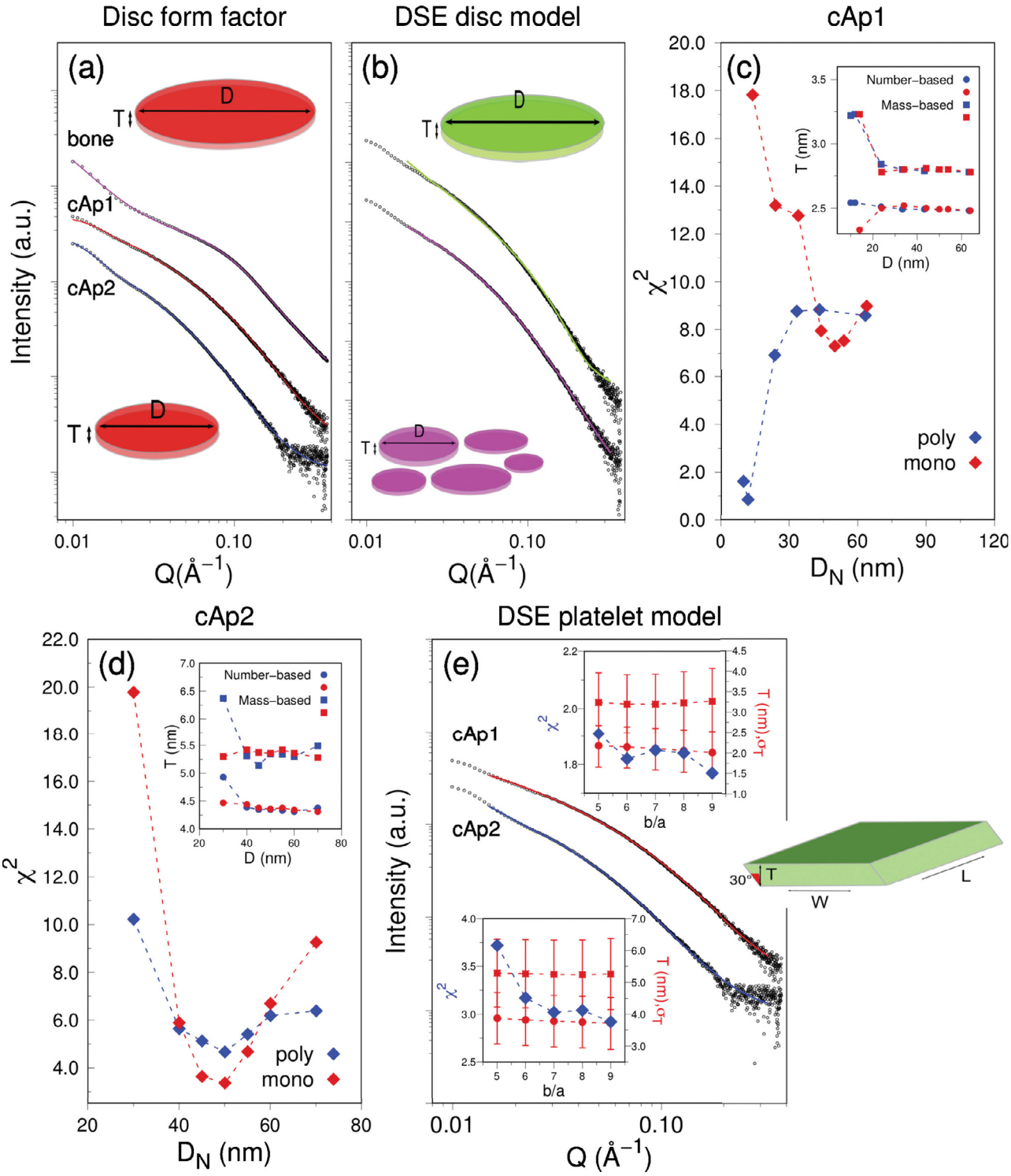

Fig. 1. (a, b, e) SAXS data (log-log scale, black dots) collected on bone and biomimetic apatite with: (a) best calculated curves from a finite disc-shape model and analytical form factors; (b) DSE best fit from atomistic disc models with mono- or polydisperse diameters for cAp1; (c, d) χ^2 *vs* diameter (D_N) for the mono- (red diamonds) and polydisperse (blue diamonds) model for cAp1 and cAp2. Relative diameter dispersions (σ_N/D_N) are provided in Tables S3-S4. Insets show the number-based (dots) and mass-based (squares) thickness for the mono (red) and the poly (blue) models; (e) DSE best fits based on atomistic models of nanoplates; insets show the χ^2 (left *y* axis, blue diamonds), thickness and standard deviation (right *y* axis, number/mass averages as red dots/squares) *vs* *b*/*a* ratio. The length of the entire vertical bars corresponds to the standard deviation (σ_T) of the thickness distribution function and not to the thickness uncertainty. Signals in (b) are shifted upwards for sake of clarity.

in both cAp1 ($\nu = 2.3$, repulsive) and cAp2 ($\nu = -0.35$, attractive) [66] in comparison to the much larger repulsive value ($\nu = 1285$) obtained for bone, likely due to dense packing on the highly mineralized collagen matrix (details are given in the Supplementary Methods). The analysis indicates opposite particle interactions in the two biomimetic samples. We hypothesize that the different behaviour may be driven by the synthesis conditions of cAp1 and cAp2, respectively, relying on diverse phosphate salts and maturation time, also affecting the crystal size and amorphous quantification (*vide infra*).

3.2.2. SAXS analysis based on the DSE method

DSE-based analysis of SAXS data relying on atomistic construction of nanocrystals has recently emerged as a complementary tool for the morphological characterization of a number of nanomaterials of technological interest [67–69]. Indeed, even though atomic scale features of nanocrystals do not contribute to the theoretical scattering curve in the Q range of SAXS data, the DSE method enables a fruitful combination of SAXS and WAXTS modelling, provided that concentration/aggregation effects can be reasonably neglected in the low-Q range (the case of highly diluted suspensions of nanoparticles) as customarily done in the high-Q range. One of the main advantages is the handling of the same size discretization (and size distribution laws) of the atomistic model that facilitates the direct comparison of size and morphological parameters from the small to the wide angle. Such advantage can be easily seen in the recent characterization of CdSe colloidal quantum dots, in which a unified atomistic model was used to fit both WAXTS and SAXS data [69].

In the present work, the DSE modelling of SAXS data was performed within a non-interfering model approximation of nanoparticles. Because of this limitation, it was only applicable (over the 0.014 – 0.33 $Å^{-1}$ Q-range) for the biomimetic cAp1 and cAp2 samples, but unfeasible for bone apatite, due to the massive concentration effects occurring in the latter (Table 1). Atomistic models of Ca deficient apatite having two different platy morphologies have been considered: 1) a disc-shape model, where polydispersity was introduced for both thickness and diameter according to a bivariate lognormal distribution. This analysis provided interesting comparison with the classical analysis, where only thickness polydispersity was considered; 2) a prismatic nanoplate model (NPL) enabling direct comparison with the morphological model used for apatite in WAXTS analysis.

Disc-shape model with thickness and diameter polydispersity. Disc-shaped apatite particles were generated by considering cylindric nanocrystals with two independent growth directions, one along the thickness T (running parallel to the c axis, with size discretization of one unit cell, *i.e.* 6.88 Å) and one in the *ab* plane (by radial increase of the diameter D of the cylindric base, with size discretization of 9.92 Å). DSE patterns were calculated for cAp1 and cAp2 in the SAXS region. Starting T values were provided by the conventional analysis (Section 3.2.1), while a grid of D spanning the 10–70 nm range was considered. For each initial (D, T) combination, differences between the calculated *vs* experimental patterns were minimized by relaxing the (number-based average) T and the standard deviations of T and D (σ_T and σ_D) according to a bivariate lognormal distribution function [21,70]. While T and σ_T were always relaxed, D and σ_D underwent two parallel strategies, one constraining σ_D/D to $\leq$1% (labelled as the *mono* strategy) and the other one relaxing the diameter polydispersity (σ_D/D to $\geq$ 20 %, labelled as the *poly* strategy).

Fig. 1b shows the best fits for cAp1 corresponding to the minima of χ^2 *vs* D displayed in Fig. 1c for the two strategies. Interestingly, the *poly* strategy allowed a lower χ^2 to be found at the smaller $D = 12.0$ nm, in combination with $\sigma_D/D \approx 50\%$ ($\chi^2_{poly} = 0.87$ *vs* $\chi^2_{mono} = 7.30$). However, when constraining the disc to nearly monodisperse diameters, the DSE modelling converged to a value of $D = 50.0$ nm, close to that provided by the conventional analysis (42.8 nm). We note that larger D combines with progressively narrower σ_D/D values (Tables S3), which further clarifies the result of conventional (relying on monodisperse diameters) *vs* DSE-based approaches.

For the cAp2 sample (Fig. 1d), the *mono* and *poly* strategies converged towards nearly equal best models featuring $D \approx 50$ nm, driven by the low diameter polydispersity ($\sigma_D/D \approx 1\%$ *vs* $\sigma_D/D \approx$ 20%, respectively) that is well described by both models. Worth of note, T is nearly unaffected by the applied strategy, as noticeable in the insets of Figs. 1c and 1d. Owing to the T polydispersity, differences must be considered regarding the number- (T_N) and mass-based (T_M) averages. For cAp1 such deviation results in $T_N \sim 2.8$ nm and $T_M \sim 3.3$ nm; for cAp2, $T_N \sim 4.3$ nm and $T_M \sim 5.3$ nm. The complete numerical outcome of these calculations is available in Tables S3-S4. Results for the best *mono* and *poly* DSE models of cAp1 and cAp2 are collected in Table 1. We observe that the different disc-shape models provide strongly homogeneous T values; slightly thinner discs are obtained by the Schulz-Zimm distribution compared to the lognormal cases. Though the deviations are very tiny (the absolute difference never exceeds 0.3 nm for T_N and 0.6 nm for T_M), the systematic effect, however, suggests a minimal dependence of T on the polydispersity function.

Prismatic nanoplatelet model. A nanoplate model having distinct and polydisperse width and length is beyond the capability of SAXS modelling due to the low information content of the data. In order to manage such a complex model and other computational issues, restraints from WAXTS analysis were applied and reasonable simplifications introduced, as follows: *(i)* we built the NPLs by conventionally adopting the same mutual orientation of apatite structure *vs* the platy morphology used in WAXTS analysis (*vide infra*); accordingly, width (W) and length (L) of NPLs were pre-assigned by aligning them to the b and c crystallographic axes, respectively, with the thickness (T) lying 30° off the a axis (in line with the hexagonal symmetry of apatite structure, as shown in the inset of Fig. 1e and Fig. 2); *(ii)* we adopted a super-cell with fixed T/W aspect ratio in the *ab* plane and *(iii)* grew prismatic NPLs by stacking the super-cell along two independent directions, one in the *ab* plane and the other one in the orthogonal direction, along the c axis. A bivariate distribution of D_{ab} (the diameter of the circle of equivalent area to the parallelogram in the *ab* plane, from which T and W are extracted) and L_c was used as a simplification of a way too complex, though more appropriate, tri-variate distribution [21].

NPLs with different supercell aspect ratios (from $b/a = 5$ to $b/a = 9$) were put in competition using suitable restraints, with the aim of obtaining values of T, W and L, to be evaluated jointly from the WAXTS data. As initial size parameters, D_{ab} were derived by combining the T_N values in Table 1 with the pertinent b/a ratio and L_c from WAXTS analysis (providing the coherent length along the c axis). D_{ab}, σ_{Dab}, L_c, σ_{Lc} (describing the bivariate population of NPLs) were then relaxed during the SAXS optimization process, with the apatite L_c from WAXTS used as the lower limit for the NPL lateral sizes. From the refined parameters, the NPL average dimensions T_X, W_X and L_X (with $X = N$ for number- and $X = M$ for mass-based values) and relative dispersions were calculated; these values are synoptically collected in Tables S5 (cAp1) and S7 (cAp2) for the different b/a ratios.

Fig. 1e summarizes the most interesting results of the NPL model for cAp1 and cAp2. These include the calculated SAXS curves (at $b/a = 7$) and, as insets, the χ^2 and thickness behaviour *vs* b/a ratio. The insets show the substantial invariance of T_N and T_M upon changing the NPL lateral sizes.

T_M are in very good agreement with the disc-shape model(s); slightly lower (model-dependent) T_N values (2.0 nm *vs* 2.5 in cAp1 and 3.8 nm *vs* 4.4 nm in cAp2) are found. In contrast to the thickness, the larger lateral sizes of the NPLs appear less robust ($W_N = 20.7$ nm for cAp1 and $W_N = 38.6$ nm for cAp2, at $b/a = 9$). This is also suggested by the rather flat behaviour of the χ^2 curves upon increasing the width, at $b/a \geq 6$. As per the NPL length, values are rather unaffected by the b/a ratio ($L_M \sim 17$ nm for cAp1, $L_M \sim 32$ for cAp2). In this respect, being SAXS "blind" to the atomic scale, the structure-morphology orientation cannot

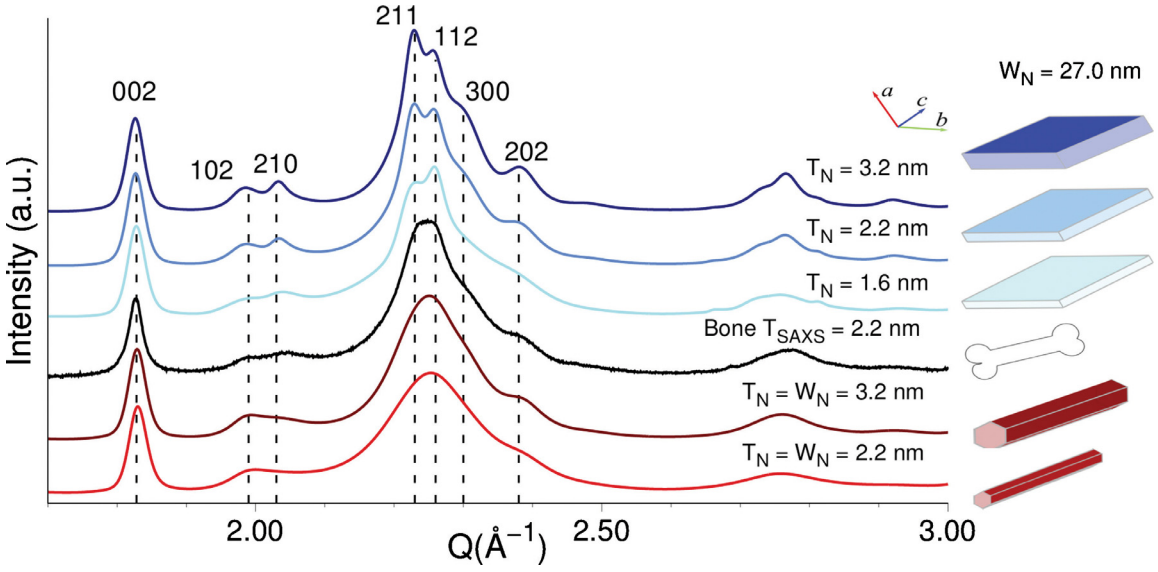

Fig. 2. X-ray synchrotron data of bone (black trace) and DSE calculations of apatite nanocrystals shaped as rods (with $W_N = T_N$) and platelets (at fixed $W_N = 27$ nm and length $L_N = 15$ nm) with variable thickness. The unit cell axes of apatite clarify the orientation of the structure vs the nanocrystal morphology. Platelets having $T_N = 2.2$ nm (blue trace) provide a pattern highly resembling the bone experimental pattern, rods of equal thickness (red trace) exhibit much broader peaks. 211 and 112 peaks of bone are smoothed out by lattice strain effects (see text for details).

be strictly derived by this analysis and switching of *W* and *L* must also be considered.

3.3. WAXTS/DSE analysis of nanocrystalline apatite

X-ray synchrotron data collected on bone, cAp1 and cAp2 (Fig. S1) in the 1.4-14 $Å^{-1}$ *Q* range, exhibit the typical features of the nanosized poorly crystalline biogenic mineral, showing substantial peak broadening mingled to significant amount of diffuse scattering. In the wide-angle region, DSE allows both the Bragg and diffuse scattering to be treated equally, based on atomistic models that convey both atomic (structure and defects) and nanometer (size and morphology) length scale features.

Model construction of apatite nanocrystals and WAXTS-DSE analysis were performed according to three major indications. (1) the clear platy morphology of the (poorly) crystalline apatite occurring both in bone and biomimetic samples. According to recent reports, the morphology of the synthetic materials (prepared in the absence of organic additives) is likely to be attributed to carbonation effects [7,21,37]. Based on DSE model calculations, in Section 3.3.1 we discuss the peculiar X-ray pattern features resulting from relevant morphological aspects of apatite nanocrystals, enabling the platy shape information to be extracted from WAXTS analysis. (2) The occurrence of additional peak broadening beyond finite-size effects. The peculiar angle-dependence suggested that this effect originated from lattice strain, likely due to the high carbonate content [7,71]. By incorporating lattice distortion in the atomistic model of apatite, as described in Section 3.3.2, a quantitative picture of lattice strain was retrieved and size- and strain-broadening effects were properly disentangled. (3) Detection of an amorphous scattering component to the diffraction pattern, both in the bone and biomimetic samples. Indeed, the strict control of the experiment, the safe subtraction of all extra-sample contributions and the DSE ability of modelling the entire scattering from the sample, overall allow the diffuse scattering originating from apatite domains to be separated from other sample scattering sources. This is the case of the amorphous layer covering the crystalline core. In this regard, since a reliable atomistic model of ACP (to be suitably juxtaposed to the crystalline part) is unavailable to date, the experimental WAXTS pattern of an ACP sample was added as a model component accounting for the amorphous part (by neglecting interference effects). The ACP signal was treated as a blank curve suitably scaled to the WAXTS pattern jointly to the DSE signal of the crystalline fraction. The scaled blank curve was fruitfully used for the ACP quantification, upon normalization to electron units; yet, its mutual spatial relationship with the crystalline part cannot be directly assessed by WAXTS. This issue is widely discussed in Section 3.4, where the quantitative results from SAXS and WAXTS analyses were suitably combined in a unified model.

Concerning the scattering from the collagen matrix in the bone sample, we show in Fig. S2 that such component can be disregarded in WAXTS modelling (as much as done in SAXS analysis), owing to the fact that the scattering from the mineral (nanocrystalline and amorphous) dominates the total measured signal.

3.3.1. On the morphology of poorly crystalline apatite from WAXTS-DSE analysis

Following the atomistic model construction of NPLs described in Section 3.2.2.2 for SAXS analysis, by varying the *b/a* ratio the apatite nanocrystals can be shaped as elongated prisms with hexagonal base (when $a = b$), or as platelets ($b/a > 1$), progressively wider upon increasing the *b/a* ratio and breaking the hexagonal structural symmetry. The way the two distinct morphologies (rod and plate) influence the wide-angle X-ray pattern of apatite has been here explored through DSE calculations, taking the diffraction pattern of the bone mineral (black trace in Fig. 2) and its thickness, provided by SAXS analysis ($T_N = 2.2$ nm, see Table 1) as reference. We show, in Fig. 2, the calculations for populations of hexagonal rods and platelets, at variable average thickness; the nanocrystals of the different populations share the same length along the *c* axis ($L_N = 15$ nm), same width ($W_N = 27.0$ nm) for platelets, and same size dispersion (~50%) along all dimensions. In order to highlight pure morphological effects, ideal defect-free nanocrystals have been used for the comparison, being lattice distortion effects treated in the next section.

We focus on those peaks mostly influenced by either the thickness of platelets/rods (30° off the *a* axis, in our NPL model), mainly 300 but also 210 and 202 reflections, or their width (running parallel to the *b* axis), namely 210, 211 and 112 reflections, at constant NPLs length. We notice that hexagonal rods with equal

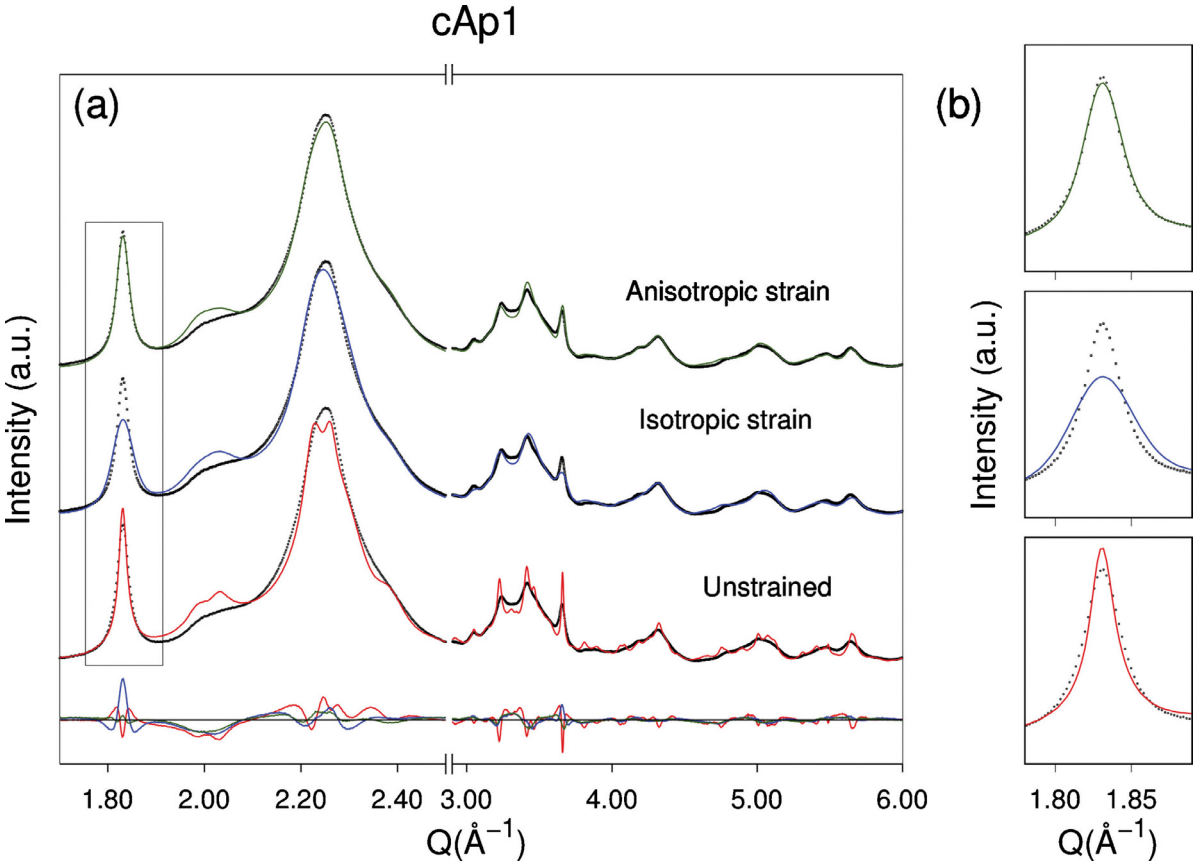

Fig. 3. (a) WAXTS data of the cAp1 (black trace) with over-imposed DSE calculated curves obtained using an unstrained model (red trace), an isotropic strain model with $\varepsilon_s = 1.0\%$ (blue trace) and an anisotropic strain model (green trace) with $\varepsilon_a \neq \varepsilon_b \neq \varepsilon_c$ (see text for details); residual profiles of each model are shown at the bottom (using the same colour code). Sizes of apatite platelets for the calculated curves and relative dispersion are collected in Table 2; (b) blow-up of the 002 peak suggesting the need of an anisotropic strain model.

($T_N = 2.2$ nm) or larger ($T_N = 3.2$ nm) thickness than in bone result in broader or even vanishing peaks, whereas detectable effects on the "thickness-sensitive" reflections are obtained by equal small variations of the NPLs thickness (± 1 nm), enabling the bone pattern features to be reproduced. Likewise, owing to the extended NPLs width, the pertinent reflections (2.2 – 2.3 Å^{-1} Q-range) become sharper and more intense and appear angularly resolved. However, we show in Fig. S3 that this feature is not significantly affected by further widening the platelets above ~10 nm, making the NPLs width the weakest morphological parameter determined by WAXTS-DSE analysis. Moreover, distinct 211 and 112 peaks are not observed in the bone trace; such discrepancy can be recovered by introducing lattice strain broadening (Fig. 3a). In summary, these findings suggest that peculiar morphological features of apatite NPLs are encoded in the WAXTS patterns (despite of the broad peaks), and that estimate of thickness, width (with some limitation) and length can be retrieved through DSE analysis of WAXTS data, upon suitable modelling. Whether the apatite platy morphology may originate from merged acicular nanocrystals, following recent scanning TEM and 3D tomographic reconstructions, cannot be ruled out [55]. Being our WAXTS data collected on randomly oriented powders, information on higher-level assembly of acicular nanocrystals into platelets is likely lost and thin platelets remain the most appropriate detectable morphology of apatite from WAXTS data. Accordingly, populations of NPLs (at different b/a ratios) exhibiting a bivariate distribution of D_{ab} and L_c were generated in order to fit WAXTS data of bone, cAp1 and cAp2. Nonetheless, as shown in Fig. 3 for cAp1, accurate morphological details did not provide exhaustive match of the experimental WAXTS patterns owing to the concomitant occurrence of size and strain broadening. We describe how the two effects have been disentangled within the DSE modelling in the following.

3.3.2. Lattice strain model of apatite NPLs through the DSE method

WAXTS analysis of bone, cAp1, cAp2 suggested that all data exhibit peak broadening beyond finite-size effects. Fig. 3a shows one of the case studies of the present work (red curves). Effects of carbonate substitution on the apatite crystal lattice are typically described in terms of detectable variation of the a and c lattice parameters [7,21], resulting in contraction of the former and expansion of the latter in the B-type replacement. Our analysis provided the following lattice parameters: $a = 9.4421(8)$ Å, $c = 6.8840(2)$ Å (bone); $a = 9.4645(6)$ Å, $c = 6.8693(2)$ Å (cAp1); $a = 9.4468(3)$ Å, $c = 6.8921(1)$ Å (cAp2). The similarity of the c values is in line with the comparable content of carbonate (Table S1) of the two biomimetic samples (in the B-type substitution) and suggests an akin carbonation level in the bone mineral [5–7]. As much as observed in the samples of this work, carbonate/phosphate replacement has also been reported in nanoapatite in relation to the broadening of Bragg peaks [71], particularly effective in the high-angle region and normally attributed to distortion of the ideal crystal periodicity originated by strain effects [72].

In this regard, due to the reported material response along the a and c axes (also supported by Molecular Dynamics simulations [7]), the carbonate/phosphate replacement is expected to intrinsically drive anisotropic lattice strain broadening [71]. Indeed, an isotropic model of lattice strain was firstly applied to our samples (by adjusting the adimensional parameter $\varepsilon_s = <\varepsilon^2>^{1/2}$, where ε

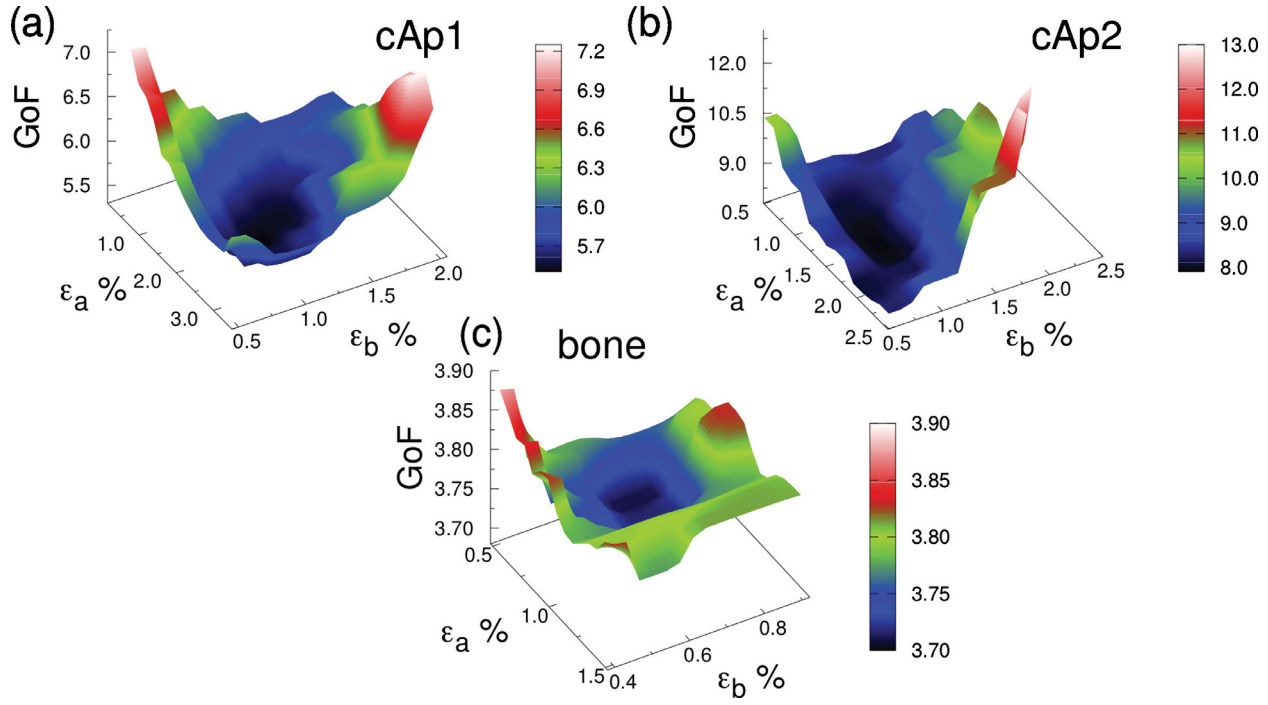

Fig. 4. (a-c) Strain analysis of cAp1, cAp2 and bone through WAXTS-DSE method; 3D hypersurface of GoF versus ε_a and ε_b for (a) cAp1 (minimum GoF = 5.51 at $\varepsilon_a = 2.2\%$, $\varepsilon_b = 1.0\%$), (b) cAp2 (GoF = 7.93 at $\varepsilon_a = 1.5\%$, $\varepsilon_b = 1.0\%$) and (c) bone (GoF = 3.74 at $\varepsilon_a = 0.9\%$, $\varepsilon_b = 0.5\%$).

$= \Delta r/r$ measures the relative radial inflation/deflation of the crystal lattice) but did not yield satisfactory fits. This result is exemplified for cAp1 in Fig. 3a and b, where the mismatch of the 002 reflection is magnified (blue curves).

An anisotropic lattice strain correction with different distortions along distinct crystallographic directions (green curves in Fig. 3a and b), was then considered based on a second-rank strain tensor. The correction was managed by introducing the lattice deformations in the atomistic model of apatite NPLs, very much as described in ref. [73]. A strain tensor accounting for three independent components along the *a*, *b* and *c* lattice parameters [$\varepsilon_a = \Delta a/a$ (ε_{11} in matrix notation) $\neq \varepsilon_b = \Delta b/b$ (ε_{22}) and $\varepsilon_c = \Delta c/c$ (ε_{33})], matching the morphological symmetry of platelets, was used. In order to find the best strain tensor coefficients, a grid search algorithm was applied exploring the goodness of fit [GoF = square root of reduced χ^2] statistical descriptor while varying the strain parameters (with a 0.05% step) in a model where the other (structural and microstructural) parameters were kept fixed. Details of the model construction, tricks used to speed up calculations and exploration of the hypersurface of GoF *vs* strain parameters are provided in the Supplementary Methods and Fig. S4.

We show in Fig. 4a-c, for cAp1, cAp2 and bone, the 3D hypersurface of GoF *vs* ε_a and ε_b with ε_c fixed at its best value (0.40% in cAp1 and bone, 0.30% in cAp2). The exploration is presented for a single *b/a* ratio for each sample. Tests indicate a minimal dependence on the *b/a* value for all strain parameters (within ±0.05%). All the maps, though characterized by relatively shallow minima, suggest a marked anisotropy of the material response along the different crystallographic directions, ε_c systematically showing the smallest (spanning in the 0.3%–0.4% range) and ε_a the largest values (0.9% in bone and up to 2.2% in the synthetic materials). These findings indicate a limited *c* axis distortion, in agreement with the apatite stiffness along this crystallographic direction found by Deymier et al. [7]. The minimum GoF of each map was obtained at the following strain parameters: $\varepsilon_a = 2.2\%$, $\varepsilon_b = 1.0\%$ for cAp1; $\varepsilon_a = 1.5\%$, $\varepsilon_b = 1.0\%$ for cAp2 and $\varepsilon_a = 0.9\%$, $\varepsilon_b = 0.5\%$ for bone (Table 2). The "optimized" lattice strains were then combined with different *b/a* ratios (from 5 to 9) for each sample and all the adjustable model parameters (sizes and dispersions, isotropic atomic thermal displacement in the form of the Debye-Waller B factor, Ca's and O_{OH} site occupancy factors (s.o.f.) were eventually relaxed.

Complete numerical results (NPLs sizes, dispersions, ACP quantification, GoF's) from this analysis are collected in Tables S6, S8-S10, from which two major findings can be highlighted: 1) upon model optimization, the NPLs construction (namely the *b/a* ratio) has a very minor influence on the final morphological and structural parameters, with the notable exception of the width (despite of comparable GoFs) (Fig. S5); 2) the NPLs thickness keeps being the most robustly determined parameter. Notably, T_M values for apatite are comparable to SAXS-determined ones for the entire NPLs, with deviations less than 0.5 nm. Since the thickness estimation is of utmost importance in studying the ACP surface layer around the apatite core by combined SAXS/WAXTS analyses, one may question about inaccurate determination of the NPLs thickness owing to possible parameters correlation effects. In this regard, additional tests were performed in order to further clarify the impact on WAXTS analysis of relevant parameters such as the thickness dispersion (σ_T), the related strain ε_a and the thickness/strain correlation.

With reference to the thickness dispersion, model optimization was replicated for each sample upon restraining σ_T/T_N to reasonably low (30%, 40%) or medium (50%, 60%) values. The most relevant results are shown in Fig. 5a-c (the complete ones are provided in Tables S11-S13); the best fitting curves in the figure refer to the minimum GoF of each sample.

The GoF plots indicate nearly unchanged $T_M \approx 3.6$ nm for bone apatite (Fig. 5c) and suggest comparable pattern matching. T_M values within ± 1.0 nm are found for the biomimetic samples (Fig. 5a-b) at relative dispersion up to 50%. These findings confirm the robustness of the (mass-based) thickness information retrieved by WAXTS analysis for apatite platelets, particularly when associated to moderate dispersions. T_N values exhibit the tendency to shrink while combining to progressively larger σ_T; averages remain within ± 1 nm.

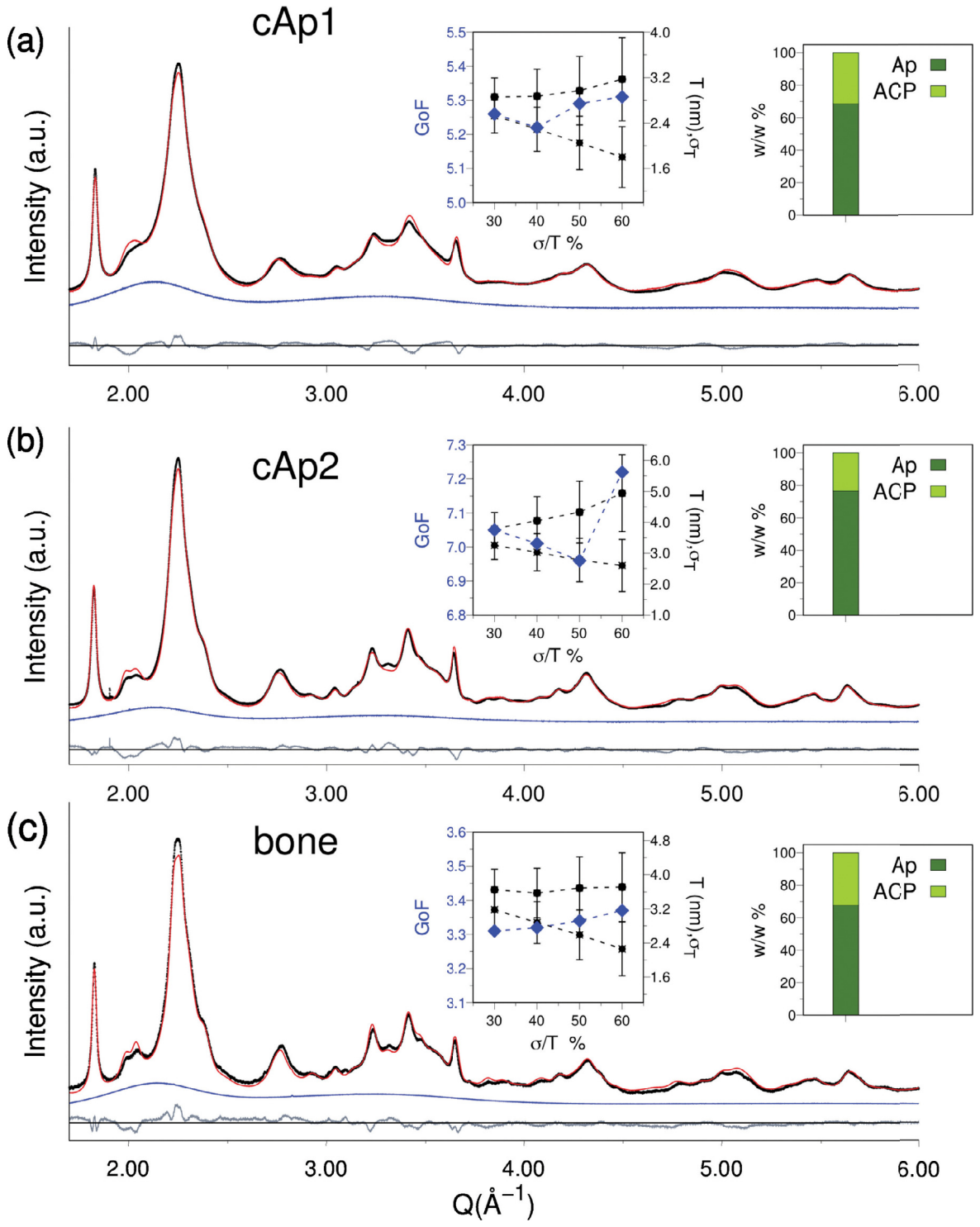

Fig. 5. WAXTS data (black dots) and best fits (red curves) provided by the DSE method using a population of apatite NPLs for (a) cAp1, (b) cAp2 and (c) bone; the blue curves describe the scattering contribution from the ACP component; the gray solid lines at the bottom show the residual between experimental and calculated pattern. Left insets: GoF versus σ_T/T_N (%) (left *y* axis, blue diamonds) and parallel T_N, T_M behaviours (right *y* axis, black squares and dots, respectively). The length of the entire vertical bars corresponds to the standard deviation (σ_T) of the thickness distribution function and not to the thickness uncertainty. Right insets: ACP and apatite (Ap) quantification for each sample.

Aiming at deeper exploring also size/strain correlation effects, an alternative strain solution was analysed for the cAp2 sample at $\varepsilon_a = 2.0\%$ (GoF = 8.18 in Fig. 4b), to be compared to the minimum of the map at $\varepsilon_a = 1.5\%$ (GoF = 7.93). Slightly larger T_N were obtained (~3.3 nm *vs* ~2.9 on average, see Table S9) upon χ^2 minimization, counterbalancing the additional strain-driven peak broadening; however, the new thickness/strain model provides slightly poorer match with the experimental data (GoF = 7.3 *vs* 7.0).

With this strategy, the best WAXTS-DSE model was selected for each sample in terms of *b/a* ratio, lattice strains, T_M, W_M, L_M and their σ values, to be used in combination with the SAXS ones. Table 2 summarizes all these values. The refined structural

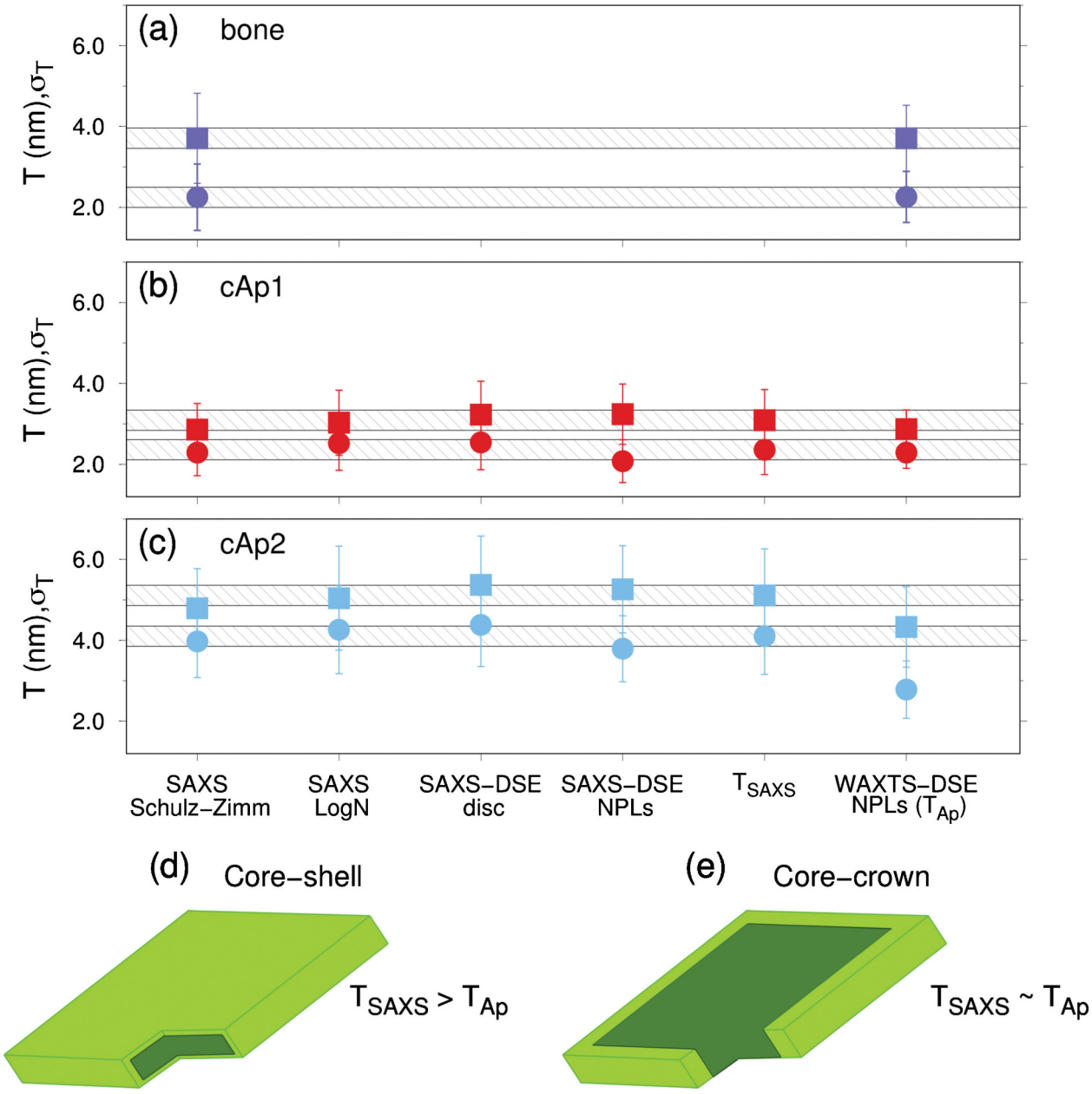

Fig. 6. Mass-averaged T_M (squares) and number-averaged T_N (dots) provided by four different SAXS models (disc-shape with Schulz-Zimm (S-Z) or lognormal (LogN) polydispersity; DSE-based disc and NPLs models) and by the WAXTS-DSE analysis, for bone (a), cAp1 (b) and cAp2 (c). T_{SAXS} refers to the average of the four models in cAp1 and cAp2, and to the S-Z for bone. Horizontal stripes 0.5 nm wide provide a reference for evaluating the T_M and T_N spreading for each sample. The length of the entire vertical bars corresponds to the standard deviation (σ_T) of the thickness distribution function and not to the thickness uncertainty. Sketches of the apatite-ACP core-shell model (d), consistent with $T_{SAXS} > T_{Ap}$, and the core-crown model (e), consistent with $T_{SAXS} \approx T_{Ap}$.

parameters (isotropic B factors and s.o.f. of Ca ions) are given in Table S14. The resulting Ca/P ratios of the apatite core are also calculated (1.61 in bone, 1.62 in cAp1 and 1.65 in cAp2). Note that the presence of the amorphous component makes these values not comparable to those (experimentally derived) reported in Table S1.

Finally, for sake of completeness, a Rietveld model is presented for the bone data in Supplementary Methods and Fig. S6. The model uses a phenomenological description of finite-size (from needle shaped crystals) and strain peak broadening (from an anisotropic strain model obeying the hexagonal apatite symmetry). The thickness of 12 nm is obtained for the needles (four times larger than the DSE nanoplates), in disagreement with SAXS results. The strain parameters (constrained to a bi-axial model) indicate a lower distortion along the *c* axis than in the *ab* plane, in line with the DSE finding.

3.4. Combining SAXS and WAXTS analyses: towards a core-crown model for bone

The results from SAXS and WAXTS analyses, previously discussed in terms of different model constructions, parameters correlations, strength and weakness points, are combined to (ideally) allocate the amorphous content around the apatite crystalline core. To this aim, highly reproducible mass-average thickness (jointly to reasonable thickness dispersions) measuring that of either the entire core-shell platelets (by SAXS, T_{SAXS} hereafter) or the apatite core (by WAXTS, T_{Ap} hereafter), and the amorphous quantification obtained through WAXTS analysis, are considered.

In this regard, we compare in Fig. 6a-c T_M and T_N values (and relative dispersions) provided by all models applied in this work to bone, cAp1 and cAp2. For bone, SAXS thickness is solely linked

to the disc-shape model with Schulz-Zimm polydispersity (Fig. 6a), which also accounts for significant concentration and aggregation effects. As deeply discussed in ref. [37], owing to these effects and the large polydispersity, some caution is suggested about the accuracy of T_{SAXS}. For the two biomimetic samples (Fig. 6b-c), the thickness values from four different SAXS models (disc-shape with Schulz-Zimm (S-Z) or lognormal (LogN) polydispersity; DSE-based disc and NPLs) agree within 0.5 nm at most, suggesting the very minor dependence of both T_M and T_N on the fitting model. However, to make further discussions independent of any specific model, T_{SAXS} is averaged over the four values and taken as reference for cAp1 and cAp2. Deviations are 0.20 nm (T_N) and 0.16 nm (T_M) for cAp1; 0.23 nm (T_N) and 0.22 nm (T_M) for cAp2, with model-dependent variations of about 4% (T_M) and 8.5% (T_N). Worth of note, mass-based values, more appropriate to treat volume-dependent properties, will be considered while discussing T_{SAXS} vs T_{Ap}.

Looking at Fig. 6a-c, we notice that T_{Ap} nearly matches T_{SAXS} in bone and cAp1, whereas a slightly larger deviation is observed in cAp2. Inspired by these findings, two alternative models may be inferred to describe the spatial relationship between the apatite core and the ACP-like surface layer, as sketched in Fig. 6d-e: 1) a core-shell like model, consistent with $T_{SAXS} > T_{Ap}$ and allocating the amorphous component homogeneously all around the crystalline core (Fig. 6d); 2) a core-crown like model, consistent with $T_{SAXS} \approx T_{Ap}$ and allocating the amorphous component mainly along the width and length edges of the crystalline core (Fig. 6e). Quantitative estimates are listed in Table 3, along with the ACP wt% provided by WAXTS analysis.

Notably, results concerning the bone sample point to the core-crown like model with a vanishing ACP-like surface layer on the basal faces of the apatite platelets. $(T_{SAXS} - T_{Ap})/T_{SAXS}$ never exceeds 6% (calculated for T_{Ap} in Tables S10 and S13). This finding envisions a spatial distribution of the disordered surface layer around the crystalline core in bone mineral that may open new scenarios on the mineral surface reactivity and crystallization/dissolution process and/or their dependence on the wet or dry state of bone. To a better comprehension of this issue, extensive studies of new bone samples, possibly at different stage of maturation, are necessary. Possible aggregation/concentration and/or model-dependent effects on the accuracy of T_{SAXS} and T_{Ap} values cannot be ruled out [37]. Nevertheless, reasonable deviations would lead, at most, to the occurrence of an ultrathin ACP-like layer (along the thickness) much thinner than the existent models (0.8 nm) [14]. Alternatively, an ultrathin disordered apatite surface preserving a high degree of coherence with the underlying crystalline arrangement may be considered and would still be consistent with the proposed model. Additional efforts are needed to further improve the current atomistic models in this direction. As per the lateral extent of the amorphous crown, a reliable estimate is difficult to recover from our combined SAXS/WAXTS analysis, owing to the limited information on the lateral size of platelets. For bone, based on the quantification of the amorphous component in Table 3 (31.6 wt%) and taking width and length from Table 2 of the apatite core, we calculate that the crown extends outwards for about 3.1 nm (1.9 nm if number-averaged values are used). Details can be found in the Supplementary Methods.

The analysis of the biomimetic samples partially confirms the bone core-crown model. Parallel results are obtained for cAp1, for which a very minor amount (~7 wt%) of the total amorphous (31.5 wt%) is covering the basal faces, the remaining fraction being able to form a ~1.2 nm wide crown. In contrast, results for cAp2 are more consistent with a core-shell like structure and a homogeneously distributed ACP-like surface layer, though slightly thinner (~ 0.4 nm on the basal faces and ~0.6 nm on the lateral ones) than the most recent reported value for bone (0.8 nm) [14]. The dissimilar amorphous location in the two biomimetic samples may be explained by the different crystallization conditions, in the presence of different cations of the phosphate salt. Indeed, apatite was detected by XRPD after 30 min of maturation in cAp2 (several hours in cAp1). The longer maturation time (96 h vs 24 h), favouring the ACP-to-apatite transformation, leads to thicker platelets and a lower amount of residual ACP (23.3 *vs* 31.5 wt%).

4. Conclusions

A complex atomic-to-nanometer scale modelling combining X-ray scattering experiments in the small and wide-angle regions has been proposed to quantitatively investigate the relationship between the crystalline apatite core and the amorphous surface layer in bone and biomimetic samples, as dry powders. According to SAXS analysis, bone mineral and synthetic materials, all exhibit a single nanoparticle morphology, consisting of thin nanoplates. According to WAXTS analysis, nanoplatelets of apatite coexist with an amorphous component and show nearly equal thickness to SAXS platelets. Overall, the results are consistent with a core-crown like structure, envisioning an alternative, never hypothesized before, spatial interconnection between the apatite core and its amorphous surface layer. These findings are of high relevance in terms of mineral surface reactivity, crystallization/dissolution process, interactions with cells and a number of extracellular components, including water, collagen, non-collagenous proteins. Extensive studies of new bone samples at different stages of maturation are necessary to corroborate the results here presented over a larger set of experimental observations. New investigations would also create the opportunity for strengthening the method and improving the models currently developed to treat this important class of biominerals. Even more detailed models treating carbonate/phosphate substitutions at the atomistic level are also of high relevance.

On the methodological side, the method here presented is able to provide a number of quantitative information of compositional, structural, defective, size and morphological nature. Results on the biomimetic samples suggest that small differences, introduced by slightly changing the synthetic conditions, can be captured by the method here proposed. This opens the way to elucidating the role that the diverse synthetic parameters may play in the crystallization process, in controlling growth and morphology of the crystalline core and the spatial location of the amorphous component. Further advances may be expected through the use of combined SAXS/WAXTS in synergy with spectroscopic techniques that have greatly raised the knowledge level in the biomineralization field.

Declaration of Competing Interest

There are no conflicts to declare. The manuscript was written through contributions of all authors. All authors have given approval to the final version of the manuscript.

Acknowledgements

This work has been performed thanks to the funding by Fondazione CARIPLO (Project No. 2016-0648: Romancing the stone: size-controlled HYdroxyaPATItes for sustainable Agriculture – HYPATIA). JMDL acknowledges FEDER/Ministerio de Ciencia, Innovación y Universidades–Agencia Estatal de Investigación (FEDER/MCIU/AEI) for partial funding through the projects NanoSmart (RYC-2016-21042) and NanoVIT (RTI-2018-095794-A-C22). GBRR also acknowledges FEDER/MCIU/AEI for her postdoctoral contract within the Juan de la Cierva Program (JdC-2017). The courtesy of the scientific and technical staff at the MS-X04A beamline of the Swiss Light Synchrotron at the Paul Scherrer Institut in Villigen, CH, is heartily acknowledged.

Supplementary materials

Supplementary material associated with this article can be found, in the online version, at doi:10.1016/j.actbio.2020.04.026.

References

[1] M.I. Kay, R.A. Young, A.S. Posner, Crystal Structure of Hydroxyapatite, Nature 204 (1964) 1050–1052.
[2] B. Wopenka, J.D. Pasteris, A mineralogical perspective on the apatite in bone, Mater. Sci. Eng. C. 25 (2005) 131–143.
[3] T. Leventouri, Synthetic and biological hydroxyapatites: crystal structure questions, Biomaterials 27 (2006) 3339–3342.
[4] G. Cho, Y. Wu, J.L. Ackerman, Detection of hydroxyl ions in bone mineral by solid-state NMR spectroscopy, Science 300 (2003) 1123–1127.
[5] L. Wang, G.H. Nancollas, Calcium Orthophosphates: Crystallization and Dissolution, Chem. Rev. 108 (2008) 4628–4669.
[6] R.Z. LeGeros, O.R. Trautz, E. Klein, J.P. LeGeros, Two types of carbonate substitution in the apatite structure, Experientia 25 (1969) 5–7.
[7] A.C. Deymier, A.K. Nair, B. Depalle, Z. Qin, K. Arcot, C. Drouet, C.H. Yoder, M.J. Buehler, S. Thomopoulos, G.M. Genin, J.D. Pasteris, Protein-free formation of bone-like apatite: New insights into the key role of carbonation, Biomaterials 127 (2017) 75–88.
[8] C. Jäger, T. Welzel, W. Meyer-Zaika, M. Epple, A solid-state NMR investigation of the structure of nanocrystalline hydroxyapatite, Magn. Reson. Chem. 44 (2006) 573–580.
[9] L. Bertinetti, A. Tampieri, E. Landi, C. Ducati, P.A. Midgley, S. Coluccia, G. Martra, Surface Structure, Hydration, and Cationic Sites of Nanohydroxyapatite: UHR-TEM, IR, and Microgravimetric Studies, J. Phys. Chem. C. 111 (2007) 4027–4035.
[10] J.M. Delgado-López, M. Iafisco, I. Rodríguez, A. Tampieri, M. Prat, J. Gómez–Morales, Crystallization of bioinspired citrate-functionalized nanoapatite with tailored carbonate content, Acta Biomater 8 (2012) 3491–3499.
[11] Y. Wang, S.V. Euw, F.M. Fernandes, S. Cassaignon, M. Selmane, G. Laurent, G. Pehau-Arnaudet, C. Coelho, L. Bonhomme-Coury, M.-M. Giraud-Guille, F. Babonneau, T. Azaïs, N. Nassif, Water-mediated structuring of bone apatite, Nature Mater 12 (2013) 1144–1153.
[12] S. Von Euw, W. Ajili, T.-H.-C. Chan-Chang, A. Delices, G. Laurent, F. Babonneau, N. Nassif, T. Azaïs, Amorphous surface layer versus transient amorphous precursor phase in bone – A case study investigated by solid-state NMR spectroscopy, Acta Biomater 59 (2017) 351–360.
[13] C. Drouet, M. Aufray, S. Rollin-Martinet, N. Vandecandelaère, D. Grossin, F. Rossignol, E. Champion, A. Navrotsky, C. Rey, Nanocrystalline apatites: The fundamental role of water, Am. Mineral. 103 (2018) 550–564.
[14] S.V. Euw, Y. Wang, G. Laurent, C. Drouet, F. Babonneau, N. Nassif, T. Azaïs, Bone mineral: new insights into its chemical composition, Sci. Rep. 9 (2019) 1–11.
[15] Y. Wu, M.J. Glimcher, C. Rey, J.L. Ackerman, A Unique Protonated Phosphate Group in Bone Mineral Not Present in Synthetic Calcium Phosphates: Identification by Phosphorus-31 Solid State NMR Spectroscopy, J. Mol. Bio. 244 (1994) 423–435.
[16] J.D. Termine, A.S. Posner, Amorphous/crystalline interrelationships in bone mineral, Calc. Tiss. Res. 1 (1967) 8–23.
[17] A.S. Posner, F. Betts, Synthetic amorphous calcium phosphate and its relation to bone mineral structure, Acc. Chem. Res. 8 (1975) 273–281.
[18] J. Mahamid, A. Sharir, L. Addadi, S. Weiner, Amorphous calcium phosphate is a major component of the forming fin bones of zebrafish: Indications for an amorphous precursor phase, P. Natl. Acad. Sci. U.S.A. 105 (2008) 12748–12753.
[19] J. Mahamid, B. Aichmayer, E. Shimoni, R. Ziblat, C. Li, S. Siegel, O. Paris, P. Fratzl, S. Weiner, L. Addadi, Mapping amorphous calcium phosphate transformation into crystalline mineral from the cell to the bone in zebrafish fin rays, Proc. Natl. Acad. Sci. U.S.A. 107 (2010) 6316–6321.
[20] G. Campi, A. Ricci, A. Guagliardi, C. Giannini, S. Lagomarsino, R. Cancedda, M. Mastrogiacomo, A. Cedola, Early stage mineralization in tissue engineering mapped by high resolution X-ray microdiffraction, Acta Biomater 8 (2012) 3411–3418.
[21] J.M. Delgado-López, R. Frison, A. Cervellino, J. Gómez-Morales, A. Guagliardi, N. Masciocchi, Crystal Size, Morphology, and Growth Mechanism in Bio-Inspired Apatite Nanocrystals, Adv. Funct. Mater. 24 (2014) 1090–1099.
[22] J.M. Delgado-Lopez, F. Bertolotti, J. Lyngso, J.S. Pedersen, A. Cervellino, N. Masciocchi, A. Guagliardi, The synergic role of collagen and citrate in stabilizing amorphous calcium phosphate precursors with platy morphology, Acta Biomater 49 (2017) 555–562.
[23] S.V. Dorozhkin, M. Epple, Biological and medical significance of calcium phosphates, Angew. Chem. Int. Ed. Engl. 41 (2002) 3130–3146.
[24] C. Rey, C. Combes, C. Drouet, H. Sfihi, A. Barroug, Physico-chemical properties of nanocrystalline apatites: Implications for biominerals and biomaterials, Mater. Sci. Eng. C. 27 (2007) 198–205.
[25] N. Nassif, F. Martineau, O. Syzgantseva, F. Gobeaux, M. Willinger, T. Coradin, S. Cassaignon, T. Azaïs, M.M. Giraud-Guille, In Vivo Inspired Conditions to Synthesize Biomimetic Hydroxyapatite, Chem. Mater. 22 (2010) 3653–3663.
[26] E.E. Wilson, A. Awonusi, M.D. Morris, D.H. Kohn, M.M.J. Tecklenburg, L.W. Beck, Three Structural Roles for Water in Bone Observed by Solid-State NMR, Biophys. J. 90 (2006) 3722–3731.
[27] M. Duer, A. Veis, Bone mineralization: Water brings order, Nat Mater 12 (2013) 1081–1082.
[28] P. Debye, Zerstreuung von Röntgenstrahlen, Ann. Phys. 351 (1915) 809–823.
[29] A. Cervellino, R. Frison, F. Bertolotti, A. Guagliardi, DEBUSSY 2.0: the new release of a Debye user system for nanocrystalline and/or disordered materials, J. Appl. Cryst. 48 (2015) 2026–2032.
[30] S. Rinnerthaler, P. Roschger, H.F. Jakob, A. Nader, K. Klaushofer, P. Fratzl, Scanning Small Angle X-ray Scattering Analysis of Human Bone Sections, Calcified Tissue Int 64 (1999) 422–429.
[31] A. Cedola, G. Campi, D. Pelliccia, I. Bukreeva, M. Fratini, M. Burghammer, L. Rigon, F. Arfelli, R.C. Chen, D. Dreossi, N. Sodini, S. Mohammadi, G. Tromba, R. Cancedda, M. Mastrogiacomo, Three dimensional visualization of engineered bone and soft tissue by combined x-ray micro-diffraction and phase contrast tomography, Phys. Med. Biol. 59 (2013) 189–201.
[32] F. Schaff, M. Bech, P. Zaslansky, C. Jud, M. Liebi, M. Guizar-Sicairos, F. Pfeiffer, Six-dimensional real and reciprocal space small-angle X-ray scattering tomography, Nature 527 (2015) 353–356.
[33] M.H. Bunger, H. Oxlund, T.K. Hansen, S. Sorensen, B.M. Bibby, J.S. Thomsen, B.L. Langdahl, F. Besenbacher, J.S. Pedersen, H. Birkedal, Strontium and bone nanostructure in normal and ovariectomized rats investigated by scanning small-angle X-ray scattering, Calcified Tissue Int 86 (2010) 294–306.
[34] N. Matsushima, M. Akiyama, Y. Terayama, Quantitative Analysis of Small-Angle X-Ray Scattering of Bone: Determination of Sizes of Its Collagen and Apatite Components, Jpn. J. Appl. Phys. 20 (1981) 699.
[35] P. Fratzl, N. Fratzl-Zelman, K. Klaushofer, G. Vogl, K. Koller, Nucleation and growth of mineral crystals in bone studied by small-angle X-ray scattering, Calcified Tissue Int 48 (1991) 407–413.
[36] P. Fratzl, S. Schreiber, K. Klaushofer, Bone mineralization as studied by small--angle x-ray scattering, Connect. Tissue Res. 34 (1996) 247–254.
[37] J.D. Kaspersen, M.J. Turunen, N. Mathavan, S. Lages, J.S. Pedersen, U. Olsson, H. Isaksson, Small-Angle X-ray Scattering Demonstrates Similar Nanostructure in Cortical Bone from Young Adult Animals of Different Species, Calcified Tissue Int 99 (2016) 76–87.
[38] A. Gourrier, C. Li, S. Siegel, O. Paris, P. Roschger, K. Klaushofer, P. Fratzl, Scanning small-angle X-ray scattering analysis of the size and organization of the mineral nanoparticles in fluorotic bone using a stack of cards model, J Appl Cryst 43 (2010) 1385–1392.
[39] C. Burger, H. Zhou, I. Sicŝ, B.S. Hsiao, B. Chu, L. Graham, M.J. Glimcher, Small--angle X-ray scattering study of intramuscular fish bone: collagen fibril superstructure determined from equidistant meridional reflections, J Appl Cryst 41 (2008) 252–261.
[40] R. Seidel, A. Gourrier, M. Kerschnitzki, M. Burghammer, P. Fratzl, H.S. Gupta, W. Wagermaier, Synchrotron 3D SAXS analysis of bone nanostructure, Bioinspired, Biomimetic and Nanobiomaterials 1 (2012) 123–131.
[41] F. Nudelman, N.A.J.M. Sommerdijk, Biomineralization as an Inspiration for Materials Chemistry, Angew. Chem. Int. Ed. Engl. 51 (2012) 6582–6596.
[42] C. Meneghini, M.C. Dalconi, S. Nuzzo, S. Mobilio, R.H. Wenk, Rietveld Refinement on X-Ray Diffraction Patterns of Bioapatite in Human Fetal Bones, Biophys. J. 84 (2003) 2021–2029.
[43] C.J.S. Ibsen, D. Chernyshov, H. Birkedal, Apatite Formation from Amorphous Calcium Phosphate and Mixed Amorphous Calcium Phosphate/Amorphous Calcium Carbonate, Chem.-Eur. J. 22 (2016) 12347–12357.
[44] N.K. Wittig, J. Palle, M. Østergaard, S. Frølich, M.E. Birkbak, K.M. Spiers, J. Garrevoet, H. Birkedal, Bone Biomineral Properties Vary across Human Osteonal Bone, ACS Nano. 13 (2019) 12949–12956.
[45] W. Wagermaier, H.S. Gupta, A. Gourrier, O. Paris, P. Roschger, M. Burghammer, C. Riekel, P. Fratzl, Scanning texture analysis of lamellar bone using microbeam synchrotron X-ray radiation, J Appl Cryst 40 (2007) 115–120.
[46] G. Campi, M. Fratini, I. Bukreeva, G. Ciasca, M. Burghammer, F. Brun, G. Tromba, M. Mastrogiacomo, A. Cedola, Imaging collagen packing dynamics during mineralization of engineered bone tissue, Acta Biomater 23 (2015) 309–316.
[47] M.E. Birkbak, H. Leemreize, S. Frølich, S.R. Stock, H. Birkedal, Diffraction scattering computed tomography: a window into the structures of complex nanomaterials, Nanoscale 7 (2015) 18402–18410.
[48] S.R. Stock, M. Laugesen, H. Birkedal, A. Jakus, R. Shah, J.-S. Park, J.D. Almer, Precision lattice parameter determination from transmission diffraction of thick specimens with irregular cross sections, J Appl Cryst 52 (2019) 40–46.
[49] M. Mastrogiacomo, G. Campi, R. Cancedda, A. Cedola, Synchrotron radiation techniques boost the research in bone tissue engineering, Acta Biomater 89 (2019) 33–46.
[50] C. Giannini, D. Siliqi, M. Ladisa, D. Altamura, A. Diaz, A. Beraudi, T. Sibillano, L. De Caro, S. Stea, F. Baruffaldi, O. Bunk, Scanning SAXS–WAXS microscopy on osteoarthritis-affected bone – an age-related study, J. Appl. Cryst. 47 (2014) 110–117.
[51] M.J. Turunen, J.D. Kaspersen, U. Olsson, M. Guizar-Sicairos, M. Bech, F. Schaff, M. Tägil, J.S. Jurvelin, H. Isaksson, Bone mineral crystal size and organization vary across mature rat bone cortex, J. Struct. Biol. 195 (2016) 337–344.
[52] D. Altamura, S.G. Pastore, M.G. Raucci, D. Siliqi, F. De Pascalis, M. Nacucchi, L. Ambrosio, C. Giannini, Scanning Small- and Wide-Angle X-ray Scattering Microscopy Selectively Probes HA Content in Gelatin/Hydroxyapatite Scaffolds for Osteochondral Defect Repair, ACS Appl. Mater. Interfaces. 8 (2016) 8728–8736.
[53] M. Albéric, A. Gourrier, W. Wagermaier, P. Fratzl, I. Reiche, The three-dimensional arrangement of the mineralized collagen fibers in elephant ivory and its relation to mechanical and optical properties, Acta Biomater 72 (2018) 342–351.

[54] P. Fratzl, M. Groschner, G. Vogl, H. Plenk, J. Eschberger, N. Fratzl-Zelman, K. Koller, K. Klaushofer, Mineral crystals in calcified tissues: A comparative study by SAXS, J. Bone Miner. Res. 7 (1992) 329–334.
[55] N. Reznikov, M. Bilton, L. Lari, M.M. Stevens, R. Kröger, Fractal-like hierarchical organization of bone begins at the nanoscale, Science 360 (2018) eaao2189.
[56] T. Egami, S.J.L. Billinge, Underneath the Bragg Peaks, Structural Analysis of Complex Materials, 2003 Kidlington, Oxford OX5 1GB, UK.
[57] A. Cervellino, R. Frison, N. Masciocchi, A. Guagliardi, X-ray powder diffraction characterization of nanomaterials, in: C.S.S.R. Kumar (Ed.), X-Ray and Neutron Techniques for Nanomaterials Characterization, Springer Berlin Heidelberg, Berlin, Heidelberg, 2016, pp. 545–608.
[58] A. Cervellino, C. Giannini, A. Guagliardi, On the efficient evaluation of Fourier patterns for nanoparticles and clusters, J. Comput. Chem. 27 (2006) 995–1008.
[59] B. Langelier, X. Wang, K. Grandfield, Atomic scale chemical tomography of human bone, Sci. Rep. 7 (2017) 1–9.
[60] J.S. Pedersen, A flux- and background-optimized version of the NanoSTAR small-angle X-ray scattering camera for solution scattering, J Appl Cryst 37 (2004) 369–380.
[61] B.H. Zimm, The Scattering of Light and the Radial Distribution Function of High Polymer Solutions, J. Chem. Phys. 16 (1948) 1093–1099.
[62] P.R. Willmott, D. Meister, S.J. Leake, M. Lange, A. Bergamaschi, M. Böge, M. Calvi, C. Cancellieri, N. Casati, A. Cervellino, Q. Chen, C. David, U. Flechsig, F. Gozzo, B. Henrich, S. Jäggi-Spielmann, B. Jakob, I. Kalichava, P. Karvinen, J. Krempasky, A. Lüdeke, R. Lüscher, S. Maag, C. Quitmann, M.L. Reinle-Schmitt, T. Schmidt, B. Schmitt, A. Streun, I. Vartiainen, M. Vitins, X. Wang, R. Wullschleger, The Materials Science beamline upgrade at the Swiss Light Source, J. Synchrotron Radiat 20 (2013) 667–682.
[63] F. Bertolotti, D. Moscheni, A. Guagliardi, N. Masciocchi, When Crystals Go Nano - The Role of Advanced X-ray Total Scattering Methods in Nanotechnology, Eur. J. Inorg. Chem. 2018 (2018) 3789–3803.
[64] S. Koutsopoulos, Synthesis and characterization of hydroxyapatite crystals: a review study on the analytical methods, J. Biomed. Mater. Res. 62 (2002) 600–612.
[65] J.S. Pedersen, Analysis of small-angle scattering data from colloids and polymer solutions: modeling and least-squares fitting, Adv. Colloid Interfac. 70 (1997) 171–210.
[66] J.S. Higgins, H.C. Benoit, Polymers and Neutron Scattering (Oxford Series on Neutron Scattering in Condensed Matter, Oxford University Press, USA, 1997.
[67] T.R. Gordon, B.T. Diroll, T. Paik, V.V.T. Doan-Nguyen, E.A. Gaulding, C.B. Murray, Characterization of Shape and Monodispersity of Anisotropic Nanocrystals through Atomistic X-ray Scattering Simulation, Chem. Mater. 27 (2015) 2502–2506.
[68] F. Bertolotti, D.N. Dirin, M. Ibanez, F. Krumeich, A. Cervellino, R. Frison, O. Voznyy, E.H. Sargent, M.V. Kovalenko, A. Guagliardi, N. Masciocchi, Crystal symmetry breaking and vacancies in colloidal lead chalcogenide quantum dots, Nat. Mater. 15 (2016) 987–994.
[69] D. Moscheni, F. Bertolotti, L. Piveteau, L. Protesescu, D.N. Dirin, M.V. Kovalenko, A. Cervellino, J.S. Pedersen, N. Masciocchi, A. Guagliardi, Size-Dependent Fault--Driven Relaxation and Faceting in Zincblende CdSe Colloidal Quantum Dots, ACS Nano 12 (2018) 12558–12570.
[70] G. Cernuto, N. Masciocchi, A. Cervellino, G.M. Colonna, A. Guagliardi, Size and shape dependence of the photocatalytic activity of TiO2 nanocrystals: a total scattering Debye function study, J. Am. Chem. Soc. 133 (2011) 3114–3119.
[71] A.A. Baig, J.L. Fox, R.A. Young, Z. Wang, J. Hsu, W.I. Higuchi, A. Chhettry, H. Zhuang, M. Otsuka, Relationships Among Carbonated Apatite Solubility, Crystallite Size, and Microstrain Parameters, Calcified Tissue Int 64 (1999) 437–449.
[72] P. Scardi, M. Ermrich, A. Fitch, E.-W. Huang, R. Jardin, R. Kuzel, A. Leineweber, A. Mendoza Cuevas, S.T. Misture, L. Rebuffi, C. Schimpf, Size–strain separation in diffraction line profile analysis, J Appl Cryst 51 (2018) 831–843.
[73] K.F. Ulbrich, F. Bertolotti, N. Masciocchi, A. Cervellino, A. Guagliardi, C.E.M. Campos, A comprehensive structural and microstructural investigation of a new iron–telluride nano phase, J. Mater. Chem. C. 6 (2018) 3047–3057.